Foundry manufacturing of octave-spanning microcombs

Jizhao Zang[1,2], Haixin Liu[1,2,*], Travis C. Briles[1], and Scott B. Papp[1,2]

[1] *Time and Frequency Division, National Institute of Standards and Technology, 325 Broadway, Boulder, Colorado 80305, USA*
[2] *Department of Physics, University of Colorado, 440 UCB, Boulder, Colorado 80305, USA*
[*] *Corresponding author: haixin.liu@colorado.edu*

Soliton microcombs provide a chip-based, octave-spanning source for self-referencing and optical metrology. We explore use of a silicon-nitride integrated photonics foundry to manufacture octave-spanning microcombs. By group-velocity dispersion engineering with the waveguide cross-section, we shape the soliton spectrum for dispersive-wave spectral enhancements at the frequencies for f-2f self-referencing. With the optimized waveguide geometry, we control the carrier-envelope offset frequency by adjusting the resonator radius. Moreover, we demonstrate the other considerations for octave microcombs, including models for soliton spectrum design, ultra-broadband resonator external coupling, low-loss edge couplers, and the nonlinear self-interactions of few-cycle solitons. This design process permits highly repeatable creation of soliton microcombs optimized for pump operation less than 100 mW, an electronically detectable offset frequency, and high comb mode power for f-2f detection. However, these design aspects must also be made compatible with the foundry fabrication tolerance of octave microcomb devices. Our experiments highlight the potential to manufacture a single-chip solution for an octave-spanning microcomb, which is the central component of a compact microsystem for optical metrology.

© 2024 Optica Publishing Group

Kerr-microresonator soliton frequency combs, or microcombs, have undergone rapid development because of the insights they provide to nonlinear dynamics and their application possibilities [1, 2]. These broadband laser sources are composed of discrete spectral lines with the relation $f_n = n f_{rep} + f_{ceo}$, where n is an integer comb mode number, f_{rep} is the repetition frequency and f_{ceo} is the carrier-envelope offset frequency. Several applications require phase stabilization of f_{rep} and f_{ceo}, including optical frequency synthesis [3] and measurement with respect to either microwave or optical clock signals, optical clock metrology, and optical frequency division [4].

Realizing a phase-stabilized microcomb involves generation of an octave-spanning spectrum with sufficient optical power for f-2f self-referencing and phase-locking of the f_{ceo} and f_{rep} signals [5]. Management of group-velocity dispersion (GVD or dispersion) is critical for all of these tasks. The spectrum of a soliton microcomb is mostly determined by the integrated dispersion, $D_{int} = \nu_\mu - (\nu_0 + \text{FSR}\,\mu)$, where μ is the relative mode number to the pump mode, ν_μ is the cold cavity reso-

nance frequency and FSR is the free spectral range at the pump [6]. While dark solitons in normal GVD have higher pump-to-comb conversion efficiency [7, 8], bright solitons in anomalous GVD offer the broadest spectra, characterized by a bandwidth adjustable mostly with the second-order dispersion parameter and coherent emission of dispersive waves (DWs) [9] that arise due to higher-order dispersion. We consider dual DW microcombs with a shortwave DW (SWDW) and a longwave DW (LWDW) at higher and lower frequency than the pump laser, respectively. These DWs are designed according to the condition $D_{int} = 0$, and they greatly enhance the comb mode power and bandwidth. We control octave microcombs mostly by adjusting D_{int} with the resonator geometry. Indeed, the SWDW and LWDW are very sensitive to fabrication tolerance. Therefore, an approximate target design exists, however, to date it has only been implemented with carefully controlled, low-volume fabrication, requiring iterative device selection and fabrication or device trimming post-fabrication [10]. For frequency metrology, foundry manufacturing as high-volume fabrication of f-2f microcombs would revolutionize use of the SI second in the optical domain.

Here, we report a single-chip solution of microcombs for f-2f self-referencing, which we fabricate at volume with a commercial silicon-nitride foundry. We present an optimized microcomb design that supports a harmonic, dual DW spectrum with an electronically accessible f_{ceo} for the highest efficiency in f-2f detection. To account for the fabrication tolerance of the foundry, a chip carries numerous resonators with a programmed variation in ring width (*RW*) and ring radius (*RR*). We model the target design according to detailed SiN dispersion engineering, optimized microcomb dynamics that enhance DW power for f-2f detection, and wavelength-dependent external resonator coupling across octave span. A new feature of our modeling is an analytical expression for the complex, octave span microcomb. Post-fabrication device screening in concert with our models characterizes the fabrication tolerance to yield optimized microcombs for f-2f detection. We demonstrate that the two DW frequencies and f_{ceo} can be independently controlled in a predictable fashion by use of resonator geometry. Finally, we discuss post-fabrication manipulation of soliton spectrum through control of the pump laser. This process reveals interesting DW dynamics that can lead to step-changes in the DW frequencies and power. Our work demonstrates a reliable procedure of generating ready-to-use octave-spanning combs through a commercial foundry, and also expands the theory of the DW dynamics
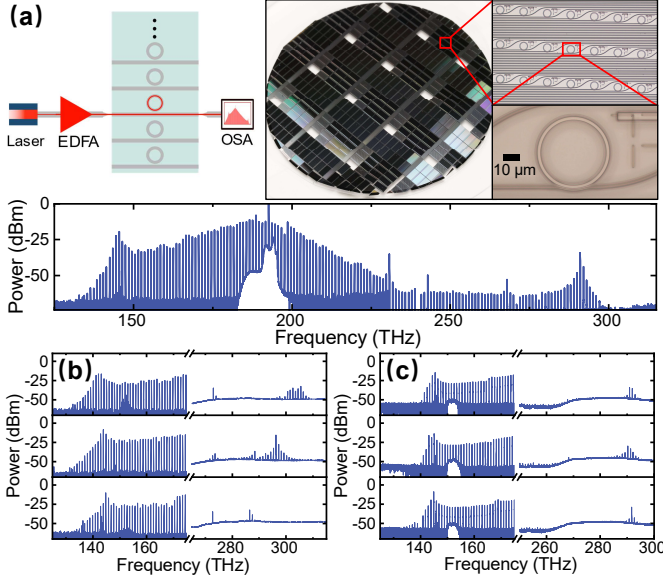
Fig. 1. Key concepts of wafer-scale search for an octave-spanning comb from commercial foundry. (a) Our chip testing setup (left) and photos of the wafer, a chip, and a resonator (clockwise from middle). The bottom spectrum shows an octave-spanning microcomb with an on-chip pump power of (151 ± 10) mW, RR of 23.475 μm, and RW of 1690 nm. (b,c) enlargements of DW spectra for different microresonator geometries. The DW locations are sensitive to RW (panel b; RW values: 1670, 1690 and 1710 nm) but less sensitive to RR (panel c; RR values: 23.475, 23.535, 23.58 μm). This allows DW control through RW and f_{ceo} control through RR.

in soliton microcombs.

We first illustrate in Fig. 1 the procedure to obtain an octave-spanning microcomb through wafer-level and chip-level device selection. The three essential parameters of our devices are layer thickness (th), RW, and RR. Before fabrication, our analytical model and simulation provided a suggested set of parameters: $th = 760$ nm, $RW = 1697$ nm, and $RR = 23.45$ μm. The devices were fabricated by Ligentec with a programmed variation in RW and RR around the suggested values. The upper inset of Fig. 1 (a) shows photos of our wafer and individual devices (right side), and our experimental setup for soliton generation and characterization (left side). The pump from a C-band continuous-wave (CW) laser is amplified by an EDFA and coupled into a microresonator chip. The chip layer is made of silicon nitride and covered by silicon dioxide top cladding, providing low edge coupling loss (< 3 dB per edge). We initiate the soliton microcombs by fast sweeping the pump frequency [11, 12], and then finely adjust the detuning to optimize two DWs, monitored by an optical spectrum analyzer (OSA). The lower inset of Fig. 1 (a) is a measured spectrum of an octave-spanning microcomb with two DWs at 145.43 THz and 290.92 THz, respectively. Figure 1 (b) and (c) show more details about how we vary RW and RR to tune the DW frequencies and f_{ceo} for a workable octave-spanning microcomb. In Fig. 1 (b), we fix RR and sweep RW from 1670 nm to 1710 nm, while in Fig. 1 (c), we fix RW and sweep RR from 23.475 μm to 23.58 μm. The measurement results indicate that the DW frequencies can be tuned by RW, and they are less sensitive to RR. On the other hand, f_{ceo} is sensitive to RR, which enables us to optimize f_{ceo} without changing the DW

frequencies. Tuning RW also changes f_{ceo} but its influence can be easily counteracted by a relatively wide scan of RR values. With the programmed variation in microresonator geometries, we can identify microcombs with an electronically accessible f_{ceo} and enhanced DWs at frequencies for f-2f self-referencing.
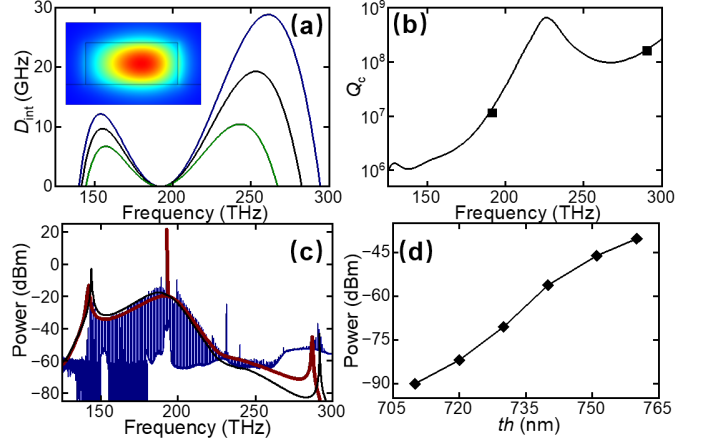

Fig. 2. Analytic model and simulation of comb spectrum. (a) The simulated D_{int} curves with $th = 760$ nm, $RR = 23.45$ μm and $RW = 1670$ nm (blue), 1697 nm (black), and 1730 nm (green). The inset shows a typical mode profile. (b) Simulated (line) and measured (squares) Q_c vs frequency for $RR = 23.535$ μm, $WGW = 500$ nm, $g_c = 950$ nm, and $L = 17$ μm. (c) A comparison among measured comb spectra (blue), prediction from our analytic approximation (black) and LLE simulation (red) with $Q_i = 1.4$M, $F^2 = 37.2$, $\alpha = 33$. (d) SWDW power vs th, predicted by our analytic model with $F^2 = 37.2$ ($P_{in} = 150$ mW) and $\alpha = 33$. For each th value, we adjust RW to ensure that the two DWs span an octave.

Next, we will discuss the steps to generate a pre-fabrication design. We first regard th as a variable. To ensure an octave span, for each th value, we find the proper RW by using COMSOL software to calculate D_{int} since DWs appear at $D_{int} \approx 0$. Figure 2 (a) shows simulated D_{int} with varied RW. The image on the left side shows a typical mode field distribution. The blue, black, and green curves plot the D_{int} with RW of 1670nm, 1697nm, and 1730nm, respectively. For the black curve, two solutions of $D_{int} = 0$ span an octave, indicating that 1697 nm is the proper RW for this th value.

After RW is determined, we design an optimal coupler that maximizes the coupling rate, denoted by $\kappa_{c\mu}$, at the SWDW, since $\kappa_{c\mu}$ is usually smaller at short wavelength. The coupling is determined by three parameters: the bus waveguide width (WGW), the gap between the bus waveguide and the ring, g_c, and the pulley length, L. We use Lumerical FDTD solver to simulate coupling quality factor, defined by $Q_c = 2\pi\nu_\mu/\kappa_{c\mu}$, and find the best values of WGW, g_c, and L. The curve in Fig. 2 (b) shows the simulated Q_c with $th = 751$ nm, $RR = 23.535$ μm, $RW = 1659$ nm, $WGW = 500$ nm, $g_c = 950$ nm, and $L = 17$ μm. The black squares are measured Q_c, which agrees well with the simulation considering the fabrication uncertainty.

We now present a quasi-analytic model for solitons generated in resonators with arbitrary D_{int} profiles and use it to quantitatively predict the spectral mode distribution of optical power, P_μ, given the device parameters and some estimation about the pump laser. This model is critical for obtaining sufficient DW power for f-2f self-referencing. Here, we define a mode-

dependent conversion efficiency $CE_\mu = P_\mu/P_{in}$, where P_{in} is the input pump power (≈ 150 mW in our experiment). P_μ can be estimated from CE_μ which is related to both the field inside the resonator and the coupling. The intracavity dynamics of Kerr microresonator is governed by the normalized LLE [13].

$$\frac{\partial E_\mu}{\partial t} = -\left(l_\mu + i\left(\alpha + D_\mu\right)\right)E_\mu + F\delta_{\mu,0} + i\sum_{\mu_1,\mu_2} E_{\mu_1}E_{\mu_2}E^*_{(\mu_1+\mu_2-\mu)}. \tag{1}$$

Here, the intracavity field is decomposed into different modes E_μ. We account for frequency dependent loss in terms of the ratio of loss rate between mode μ and the pump ($\mu = 0$), $l_\mu = (\kappa_{i\mu} + \kappa_{c\mu})/(\kappa_{i0} + \kappa_{c0})$, where $\kappa_{i\mu}$ is the intrinsic loss rate. α is the detuning of the pump laser, normalized by the halfwidth of pump mode $(\kappa_{i0} + \kappa_{c0})/(4\pi)$. $D_\mu = 4\pi D_{int}/(\kappa_{i0} + \kappa_{c0})$ is the normalized D_{int}. F is the normalized driving force and related to P_{in} and threshold power P_{thre} by $F^2 = P_{in}/P_{thre}$.

The relation between coupling and CE_μ is characterized by $r_\mu = 2K_\mu/(K_\mu + 1)$ where $K_\mu = \kappa_{c\mu}/\kappa_{i\mu}$ is the coupling coefficient of mode μ, and CE_μ has the following form [13]:

$$CE_\mu = \frac{|E_\mu|^2 l_\mu r_\mu}{F^2/r_0} \times \frac{\omega_\mu}{\omega_0}, \tag{2}$$

where ω_μ is the output angular frequency of mode μ. As discussed above, $\kappa_{c\mu}$ can be calculated from Q_c. While Q_c varies greatly over frequency, the intrinsic quality factor $Q_i = 2\pi\nu_\mu/\kappa_{i\mu}$ has much smaller variation. We assumed Q_i to be a constant measured in previous fabrication. Then, l_μ and r_μ can be calculated from Q_c. Equation 2 suggests that we can calculate CE_μ if we know E_μ and F. In resonators with low loss and purely quadratic dispersion, $D_\mu = d_2\mu^2/2$, the soliton spectra is approximated by [14]:

$$E_\mu^{(0)} = \frac{\sqrt{d_2}}{2}\text{Sech}\left[\frac{\pi}{2}\sqrt{\frac{d_2}{2\alpha}}\mu\right]. \tag{3}$$

For non-quadratic dispersion, currently no model can approximate the soliton spectra. Here, we provide two extra orders of correction for E_μ which can characterize the spectrum around DWs through perturbation method. To distinguish Eqn. 3 from our correction, we denote it with a superscript (0).

Our model assumes that $D_\mu \approx d_2\mu^2/2$ for small μ but diverges from quadratic shape at large μ. For a steady comb, $\partial E_\mu/\partial t = i\lambda E_\mu$, where λ is the time rate of change of the phase and equals the difference between f_{rep} and FSR. For a D_{int} with even parity, $\lambda = 0$. We assume $\lambda = 0$ in our model but will discuss later that nonzero λ will result in DW switching phenomenon. As a result, for nonzero μ, we rewrite Eqn. 1 into:

$$E_\mu = \frac{\sum_{\mu_1,\mu_2} E_{\mu_1}E_{\mu_2}E^*_{(\mu_1+\mu_2-\mu)}}{-il_\mu + \alpha + D_\mu}. \tag{4}$$

With this equation, we can calculate our first order solution $E_\mu^{(1)}$ by replacing E_μ on the right side with $E_\mu^{(0)}$. Instead of directly doing the summation, a more clever way is to notice that $E_\mu^{(0)}$ is a good approximation when D_μ is exactly $d_2\mu^2/2$. So, according to Eqn. 4, $\sum_{\mu_1,\mu_2} E_{\mu_1}^{(0)}E_{\mu_2}^{(0)}E_{(\mu_1+\mu_2-\mu)}^{(0)*} \approx (-il_\mu + \alpha + d_2\mu^2/2)E_\mu^{(0)}$, and $E_\mu^{(1)}$ has the following expression:

$$E_\mu^{(1)} = c_\mu^{(1)}E_\mu^{(0)}, \quad c_\mu^{(1)} = \frac{-il_\mu + \alpha + d_2\mu^2/2}{-il_\mu + \alpha + D_\mu}, \tag{5}$$

where $c_\mu^{(1)}$ is the first order correction. This expression already gives insight into comb power distribution across a dispersion profile. A striking feature of DWs is that P_μ has local maximum at modes where $D_{int} \approx 0$. This is explained by Eqn. 5: for most modes, $D_\mu \gg \alpha, l_\mu$, and $|c_\mu^{(1)}|^2$ is relatively small, but when D_μ decreases to $-\alpha$, the lineshape of $|c_\mu^{(1)}|^2$ becomes a Lorentzian with peak value $\approx \left(d_2\mu^2/(2l_\mu)\right)^2$.

A more accurate spectrum needs the second order correction:

$$E_\mu^{(2)} = E_\mu^0 \frac{\sum_{\mu_1,\mu_3} c_{\mu_1}^{(1)} c_{(\mu_3-\mu_1)}^{(1)} c_{(\mu_3-\mu)}^{(1)*} E_{\mu_1}^{(0)} E_{\mu_3-\mu_1}^{(0)} E_{(\mu_3-\mu)}^{(0)*}/E_\mu^{(0)}}{-il_\mu + \alpha + D_\mu}. \tag{6}$$

Note that $\text{Sech}[x] \leqslant 2\,\text{Exp}[-|x|]$ and $|\mu_1| + |\mu_3 - \mu_1| + |\mu_3 - \mu| \geqslant |\mu|$. $E_{\mu_1}^{(0)} E_{\mu_3-\mu_1}^{(0)} E_{(\mu_3-\mu)}^{(0)*}/E_\mu^{(0)}$ vanishes exponentially except for the case where $\mu \leqslant \mu_3 \leqslant \mu_1 \leqslant 0$ or $\mu \geqslant \mu_3 \geqslant \mu_1 \geqslant 0$, and $E_{\mu_1}^{(0)} E_{\mu_3-\mu_1}^{(0)} E_{(\mu_3-\mu)}^{(0)*}/E_\mu^{(0)} \approx d_2$. Then $E_\mu^{(2)}$ can be expressed as:

$$E_\mu^{(2)} = c_\mu^{(2)} c_\mu^{(1)} E_\mu^{(0)}, c_\mu^{(2)} = \frac{-il_\mu + \alpha + d_2\sum_{\mu_1,\mu_3} c_{\mu_1}^{(1)} c_{\mu_3-\mu_1}^{(1)} c_{(\mu_3-\mu)}^{(1)*}}{-il_\mu + \alpha + d_2\left(|\mu|+1\right)\left(|\mu|+2\right)/2}, \tag{7}$$

where the summation is done over $\mu \leqslant \mu_3 \leqslant \mu_1 \leqslant 0$ or $\mu \geqslant \mu_3 \geqslant \mu_1 \geqslant 0$. In $c_\mu^{(2)}$, we retain $-il_\mu + \alpha$ in the numerator, and replace $\mu^2/2$ with $(|\mu|+1)(|\mu|+2)/2$. This modification makes $c_\mu^{(2)}$ converge to 1 when $c_\mu^{(1)} = 1$.

Using Eqn. 2 and 7, we can calculate the spectrum of output comb with given values of D_μ, l_μ, r_μ, F, α and P_{in}. Equation 3 indicates that larger α leads to more power, as observed in experiment as well. While absent from Eqn. 7, F^2 affects P_μ indirectly by altering the soliton existence range, for which the upper bound of α is $\pi^2 F^2/8$ [14]. During the design, we set F based on our laser power and the measured P_{thre}, and perform numerical simulation with Matlab, based on Eqn. 1 directly, to estimate the maximum α and the comb spectrum more accurately. Figure 2 (c) is a comparison among our analytic approximation (black curve), LLE simualtion (red curve), and measured spectrum (blue trace) with nominal RW and th to be 1690 nm and 760 nm, respectively. For the analytic approximation and numerical simulation, we use the same device parameters as in Fig. 2 (b) and Q_i is 1.4M. Considering the fabrication uncertainty, the analytic, simulated and experimental spectra agree well.

The last parameter to optimize is th. We calculate the SWDW power versus th using our analytic model, shown in Fig. 2(d). Here, we set $RR = 23.45$ μm, $P_{in} = 150$ mW, $F^2 = 37.2$, and $\alpha = 33$. RW is adjusted to keep an octave span of DWs. It shows that $th = 760$ nm will yield the highest SWDW power.

With the suggested device parameters, we next determine their sweep ranges based on the sensitivity of DWs and f_{ceo}. To characterize the harmonic mismatch between two DWs, we define the quantity $2\nu_L - \nu_S$, where ν_L and ν_S are LWDW and SWDW frequencies, and plot it as a function of RW and th with a fixed $RR = 23.5$ μm (Fig. 3 (a)). The green, black, and red curves with diamonds show the theoretical values with $th = 754$ nm, 760 nm and 766 nm, respectively. The blue squares are calculated from measured ν_L and ν_S. The plot shows that 1 nm uncertainty in th requires 5 nm sweep in RW to compensate.

Figure 3 (b) plots the theoretical (black curve with diamonds) and measured (black squares) f_{ceo} over RR with $RW = 1690$ nm and $th = 760$ nm. The lowest measured f_{ceo} is 5.1 GHz with $RR = 23.535$ μm and the corresponding spectrum is shown in
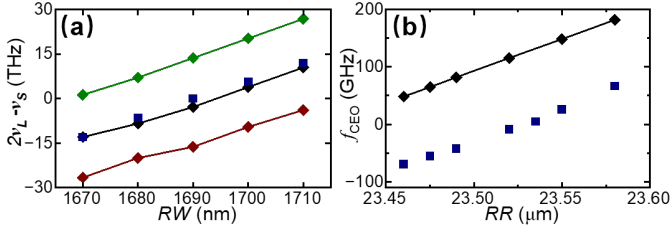
Fig. 3. Tuning of DW frequencies and f_{ceo} (a) $2\nu_L - \nu_S$ vs RW for th = 754 nm (green), 760 nm (black) and 766 nm (green). The blue squares show the measured data for th = 760 nm. (b) Simulated (black curve with diamonds) and measured (blue squares) f_{ceo} as a function of RR.

Fig. 2 (c). Despite an overall shift between prediction and experimental result due to fabrication tolerance, the similar linear dependence and slope over RR highlight the accuracy of our prediction. Since f_{ceo} is always less than FSR (~ 1 THz), a sweep range of 0.8 μm in RR will always compensate the fabrication uncertainties and enable an electrically accessible f_{ceo}.
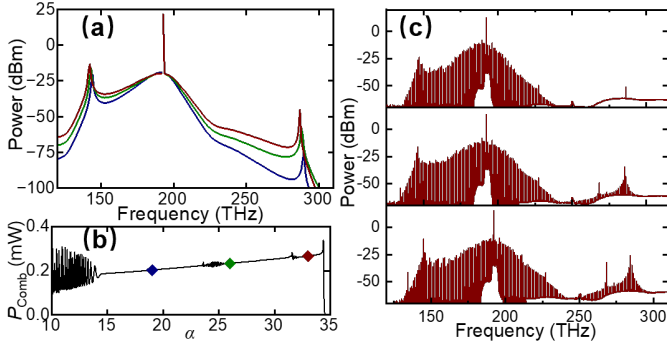

Fig. 4. Dependence of comb spectrum on pump laser. (a) Simulated soliton spectra with $F^2 = 37.2$, $\alpha = 19$ (blue), 26 (green), and 33 (red) using resonator parameters from Fig. 2 (c) except α. (μ_L, μ_S) are (-51,102) (blue), (-52,100) (green), and (-53,99) (red). (b) Simulated comb power as a function of α. Each colored diamond corresponds to the soliton spectrum with the same color in (a). (c) Measured soliton spectra with the same devices but different P_{in}: 74 mW (top), 89 mW (middle), and 126 mW (bottom).

Besides device design, we can also use post-fabrication methods to manipulate soliton spectrum through control of the pump laser. Here, we investigate how α and P_{in} affect DWs and the DW switching phenomenon. According to Eqn. 3, α determines the attenuation rate of P_μ versus μ. In addition, we found both in experiment and simulation that DWs might switch from one mode to another nearby mode during the detuning sweep, enabling fine tuning of DW frequencies. This behavior comes from the nonlinear self-interactions between DWs and its parent soliton, causing f_{rep} to diverge from FSR [15], namely $\lambda \neq 0$, which can be regarded as an effective shift in D_{int} and switches DW modes. In Fig. 4 (a), we plot three LLE-simulated spectra with varied α: 19 (blue), 26 (green) and 33 (red) ($F^2 = 37.2$). The simulated comb power P_{comb} versus α is shown in Fig. 4 (b), where the corresponding α for each spectrum in Fig. 4 (a) is indicated by diamonds in the same color. Each comb is a stable solution of LLE and we have experimentally verified that these states correspond to low noise combs [5]. The relative mode

numbers of DWs (μ_L, μ_S) switch from (-51,102) (blue) to (-52,100) (green), and then to (-53,99) (red). In contrast to quadratic GVD combs, P_{comb} does not increase smoothly in Fig. 4 (b). Instead we observe that P_{comb} vs α behavior is interrupted by high noise regions around $\alpha = 25$ and 32. These regions are related to the intracavity dynamics of DWs that cause jumps of DW frequency and power [15].

As mention above, P_{in} can also affect CE_μ by affecting the range of α where the soliton can exist. Figure 4 (c) plots three measured spectra from the same device but with increasng P_{in}: 74 mW, 89 mW, 126 mW. For each P_{in}, we tuned α to maximize the SWDW power in experiment. While P_{in} increases by less than two times, the SWDW power increases by tens of dB, which we attribute to a larger α able to support the soliton.

In summary, microresonator-based optical frequency combs are promising for chip-scale integration and low-power operation but suffer from the high sensitivity to the fabrication process. Benefiting from the consistent fabrication tolerance of a commercial foundry, we demonstrate a systematical design process and wafer-scale search method to achieve octave-spanning combs with an electrically detectable f_{ceo} (5.1 GHz). We also provide an analytical model to predict the soliton spectrum with two DWs and investigate its dependence on the device parameters as well as the pump laser. The experiment results agree well with this analytical model and LLE simulations. Our work represents an important step towards the practical applications of the microresonator-based octave-spanning combs for self referencing.

Disclosures. The authors declare no conflicts of interest.

REFERENCES

1. T. J. Kippenberg, A. L. Gaeta, M. Lipson, and M. L. Gorodetsky, Science **361** (2018).
2. A. L. Gaeta, M. Lipson, and T. J. Kippenberg, Nat. Photonics **13**, 158 (2019).
3. D. T. Spencer, T. Drake, T. C. Briles, *et al.*, Nature **557**, 81 (2018).
4. S. Sun, B. Wang, K. Liu, *et al.*, Nature pp. 1–6 (2024).
5. T. C. Briles, J. R. Stone, T. E. Drake, *et al.*, Opt. Lett. **43**, 2933 (2018).
6. J. A. Black, G. Brodnik, H. Liu, *et al.*, Optica **9**, 1183 (2022).
7. G. Spektor, J. Zang, A. Dan, *et al.*, APL Photonics **9** (2024).
8. J. Zang, S.-P. Yu, H. Liu, *et al.*, arXiv preprint arXiv:2401.16740 (2024).
9. V. Brasch, M. Geiselmann, T. Herr, *et al.*, Science **351**, 357 (2016).
10. G. Moille, D. Westly, E. F. Perez, *et al.*, APL Photonics **7** (2022).
11. J. R. Stone, T. C. Briles, T. E. Drake, *et al.*, Phys. Rev. Lett. **121**, 063902 (2018).
12. T. C. Briles, S. P. Yu, T. E. Drake, *et al.*, Phys. Rev. Appl. **14**, 1 (2020).
13. H. Liu, G. M. Brodnik, J. Zang, *et al.*, Phys. Rev. Lett. **132**, 023801 (2024).
14. T. Herr, V. Brasch, J. D. Jost, *et al.*, Nat. Photonics **8**, 145 (2014).
15. D. V. Skryabin and Y. V. Kartashov, Opt. Express **25**, 27442 (2017).